Technical Article

Enhancing electrical machine design through hybrid numerical techniques and pareto optimization strategies

Abstract — **Recent trends in electrical machine design focus on implementation of advanced materials and efficiency maximization in conjunction with other criteria such as power density increase and high reliability achievement necessitating composite cost functions consideration. Neodymium alloy permanent magnet developments enabled winding replacement resulting in the respective copper loss reduction and are favored in traction applications. However, neglecting the permanent magnet loss at the design stage and adopting fixed weights on composite cost function components during the optimization procedure may lead to substantial suboptimal characteristics. In order to overcome this difficulty, particular methodologies are proposed enabling permanent magnet loss consideration based on hybrid numerical techniques and adequate contradictory criteria satisfaction by using pareto evolutionary optimization algorithms, illustrated through several traction motor application examples.**

I. INTRODUCTION

Permanent magnet motors have been widely used in electric traction applications due to their inherent advantages of avoiding the respective copper losses and enabling high performance and power density. The nature of the application specifications, regarding both performance and efficiency, in conjunction with the needs for high power quality and reduced weight, have highlighted the necessity for the thorough investigation of their operational characteristics and behavior as well as their systematized optimization [1],[2].

In recent bibliography, in order to avoid subjective fixed weights in composite cost functions, several techniques emphasizing on multi-objective strategies have been proposed for motor optimization in electric traction applications. In [3] a multi-objective Differential Evolution (DE) technique is employed for the optimization of a PM actuator, while in [4] a multi-objective approach combining DE with concepts from Strength Pareto Evolutionary Algorithm (SPEA) is applied to an electromagnetic optimization problem. In [5], [6] a modified imperialist competitive algorithm and a bat-inspired optimization methodology, respectively, are employed for the optimization of a brushless DC wheel motor system. In [7] PM motors with soft composite cores are optimized using NSGA 2, while in [8] a particle swarm optimization technique is utilized to increase the efficiency of the powertrain system of a hybrid electric vehicle. Finally, in [9] a multi-objective evolutionary optimization methodology, employing a mesh refinement technique is presented.

Surface mounted permanent magnet motors involving important over-torque capability are favored in many applications. In such cases, however, the permanent magnet eddy losses are important, especially in higher speed ranges [10],[11], and is worth to be considered at the design stage. It is possible to reduce them by applying magnet segmentation with some compromise in torque density [12]-[17]. Consideration of permanent magnet losses by finite element techniques is very demanding in computation time [18] and difficult to implement in geometry optimization procedures [19]. In order to overcome such a difficulty, permanent magnet eddy current losses consideration by using hybrid numerical techniques based on a conveniently coupling of finite element models with analytical solutions is proposed. Such modeling procedures combined with pareto front evolutionary algorithms constitute powerful design methodologies for Surface Mounted Permanent Magnet (SMPM) motors optimization.

II. MODELING OF PERMANENT MAGNETS

Analytical solutions for eddy current problems of different configurations have extensively been developed in the literature [20]. The analysis of surface mounted permanent magnets has been base on a particular two dimensional representation involving cylindrical coordinate system.

A. Representation of eddy current losses by analytical solutions

The adopted analytical model for a surface mounted magnet on the rotor with pitch α_p is based on a two dimensional machine configuration as shown in Fig. 1.

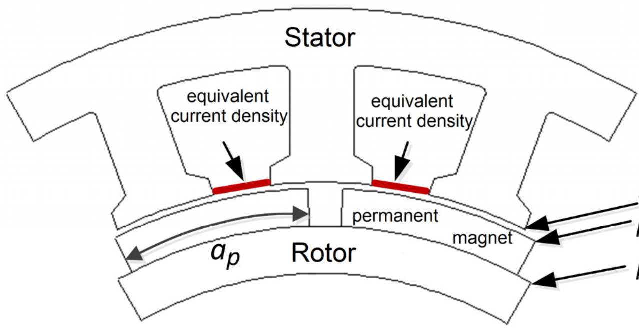

Fig. 1. Surface mounted permanent magnet machine configuration.

The analysis is based on a representation of the stator ampere-turns distribution by an equivalent current sheet of infinitesimal thickness disposed over the slot opening [21]. For the needs of the analysis, only the fundamental of the line current, is calculated from the finite element model, while the respective equivalent current sheet $J=H_t$ is evaluated through the normal derivative of the vector potential A along the slot opening, as follows:

$$H_t = -\frac{1}{\mu_0}\frac{\partial A}{\partial r} \quad (1)$$

If the slot opening has a width β_0 then the equivalent current density distribution along the stator surface for one slot with total current I and two slots with total currents I and $-I$, respectively, are shown in Fig. 2. The distributions of phase conductors in the slots and the corresponding current densities along stator surface for the cases of full pitch three phase single layer winding, fractional slot single layer winding and fractional slot two layer winding, are shown in Figs. 3a, 3b and 3c, respectively. The equivalent current density along stator surface J_s for the standard three phase single layer winding is given in (2):

$$J_s(\alpha,R_s,t)=\sum_u^{\infty}\sum_v^{\infty}\mp\frac{2N_{ph}I_u}{\pi R_s}K_{wn}K_{sov}\cos\left[up_r\omega_r t\pm v\alpha+\theta_u\right] \quad (2)$$

where N_{ph} is the number of turns in series, u is the time harmonic order and v is the space harmonic order satisfying the relations:

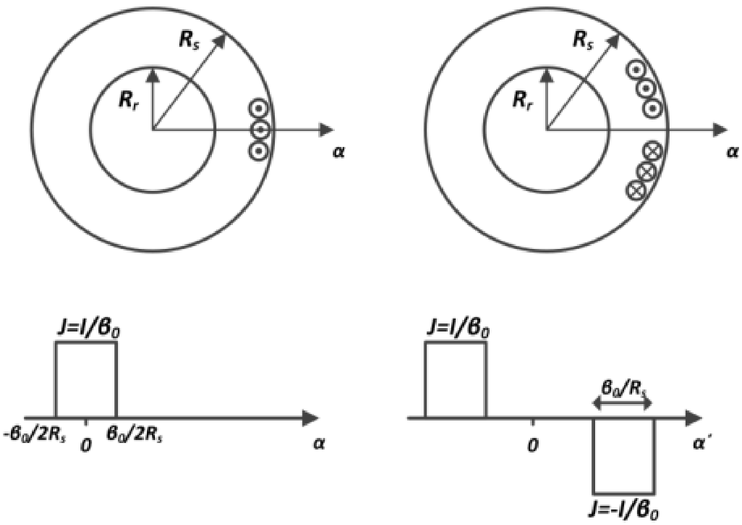

Fig. 2. Representation of the equivalent current density J distribution along the stator surface of the machine with one with current I and two slots with currents I and –I, respectively.

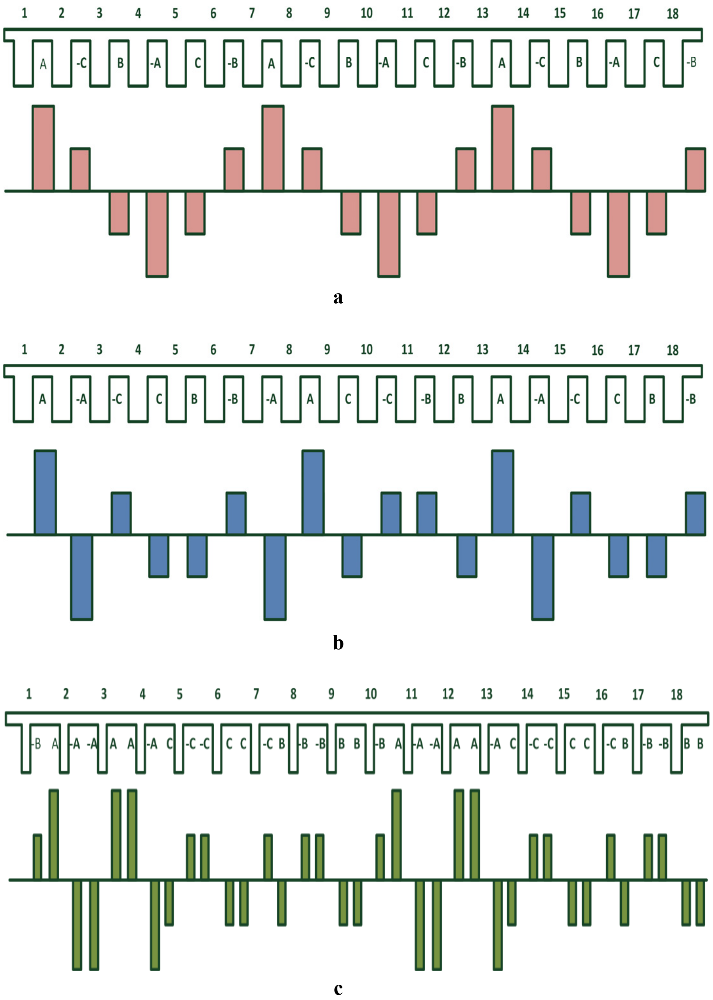

Fig. 3. Distributions of phase conductors in the slots of a stator with 18 slots per pole pair and the respective equivalent current density.
a: Concentrated Single layer three phase stator winding
b: Fractional slot single layer stator winding
c: Fractional slot double layer stator winding.

$$\begin{aligned} v&=3c\pm u,\\ c&=0,\pm1,\pm2,\ldots \end{aligned} \quad (3)$$

while K_{wv} is the winding factor and K_{sov} is the slot opening factor for the v_{th} space harmonic. The eddy current density in the magnets can then be expressed as follows:

$$J_m(r,\theta_r,t)=-\frac{i}{\rho}\frac{\partial A}{\partial t}+C(t) \quad (4)$$

where $C(t)$ is an integration constant ensuring that the total current density within a magnet segment is zero. The eddy current losses in the magnets can then be calculated as follows:

$$P_{ed}=2p_r\frac{\omega_r}{2\pi}\int_0^{2\pi/\omega_r}\int_{R_m}^{R_r}\int_{-\alpha/2}^{\alpha/2}\rho J_m^2\,r\,dr\,d\theta_r\,dt=\sum_u\sum_v\left(P_{cuv}+P_{auv}\right) \quad (5)$$

where ρ is the permanent magnet resistivity. The terms P_{cuv} and P_{auv} are given by the following expressions:

$$\begin{aligned} P_{cuv}&=\frac{q^2\mu_o^2a_pp_rl_a}{8\rho}\sum_u^{\infty}\sum_v^{\infty}\frac{J_n^2}{v^2p_s^2}(up_r\mp vp_s)^2\omega_r^2\\ &\times\left[\left(\frac{R_m}{R_s}\right)^{2vp_s}\frac{R_s^2R_m^2}{(2vp_s+2)}\left(1-\left(\frac{R_r}{R_m}\right)^{2vp_s+2}\right)\right.\\ &\left.+\left(\frac{R_r}{R_s}\right)^{2vp_s}R_s^2R_r^2F_v+\left(\frac{R_r}{R_s}\right)^{2vp_s}R_s^2\left(R_m^2-R_r^2\right)\right]\\ &\times\left[1-\left(\frac{R_r}{R_s}\right)^{2vp_s}\right]^{-2} \end{aligned} \quad (6)$$

where the function F_v is of the form:

$$F_v=\begin{cases}\dfrac{\left[\left(\dfrac{R_m}{R_r}\right)^{-2vp_s+2}-1\right]}{(-2vp_s+2)} & \text{when } vp_s\neq 1\\[2ex] \ln\left(\dfrac{R_m}{R_r}\right) & \text{when } vp_s=1\end{cases} \quad (7)$$

And the term P_{auv} is given by the expression:

$$\begin{aligned} P_{auv}&=-\frac{q^2\mu_o^2p_rl_a}{a_p\rho}\sum_u^{\infty}\sum_v^{\infty}\frac{J_n^2}{v^4p_s^4}(up_r\mp vp_s)^2\omega_r^2\\ &\times\left[\left(\frac{R_m}{R_s}\right)^{vp_s}\frac{R_sR_m^2}{(vp_s+2)}\left(1-\left(\frac{R_r}{R_m}\right)^{vp_s+2}\right)+\left(\frac{R_r}{R_s}\right)^{vp_s}R_sR_r^2G_v\right]^2\\ &\times\frac{\sin^2(vp_s\frac{a_p}{2})}{(R_m^2-R_r^2)\left[1-\left(\frac{R_r}{R_s}\right)^{2vp_s}\right]^2} \end{aligned} \quad (8)$$

where the function G_v is of the form:

$$G_v=\begin{cases}\dfrac{\left[\left(\dfrac{R_m}{R_r}\right)^{-vp_s+2}-1\right]}{(-vp_s+2)} & \text{when } vp_s\neq 2\\[2ex] \ln\left(\dfrac{R_m}{R_r}\right) & \text{when } vp_s=2\end{cases} \quad (9)$$

B. Impact on losses of permanent magnet segmentation

As an example a 10 pole surface mounted permanent magnet machine has been considered with 12 stator slots with N_{ph}=42, q=3 slots per pole and phase, R_s=0,0165 m, R_m=0,0157 m, R_r=0,0117 m, ρ=1,441·10^{-6} S και I_m=20 A. The equivalent current density distributions along the stator surface for single layer stator winding and double layer stator winding are shown in Figs. 4 and 5, respectively. Moreover, the calculated flux density distribution in the air-gap for the two considered winding configurations are shown in Figs. 6 and 7, respectively.

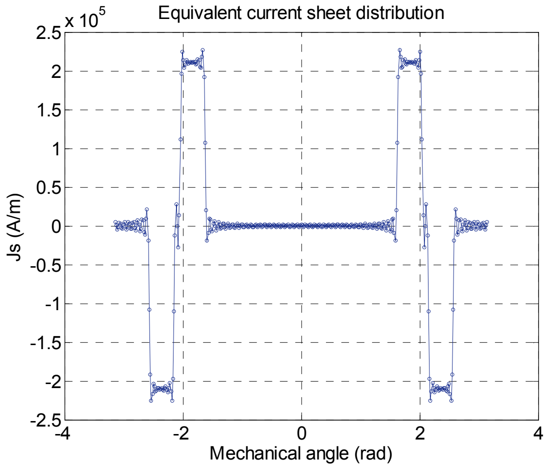

Fig. 4. Equivalent current sheet distributions along the stator surface in case of fractional slot single layer stator winding

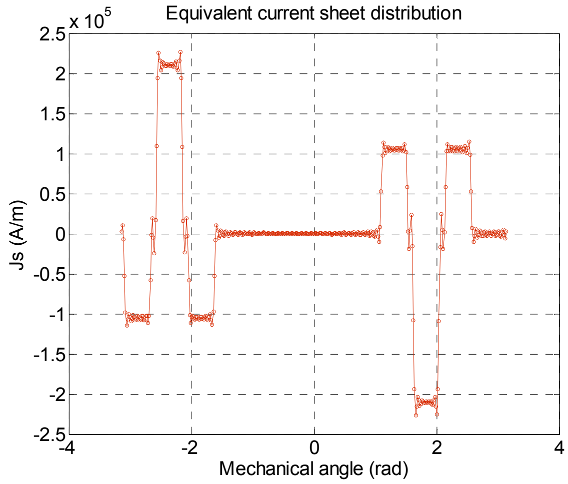

Fig. 5. Equivalent current sheet distributions along the stator surface in the case of fractional slot double layer stator winding.

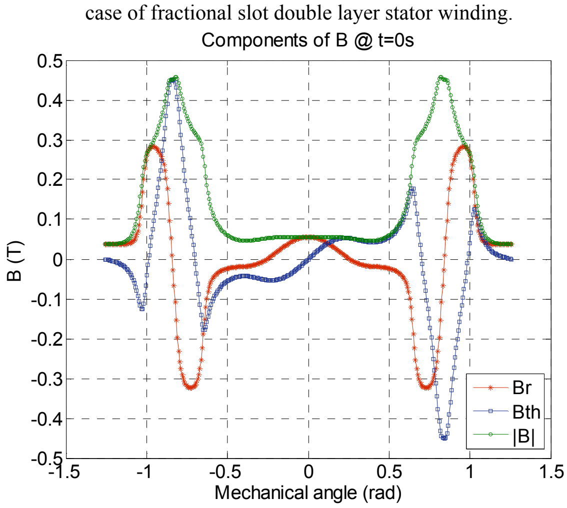

Fig. 6. Flux density components distribution in the air gap surface in case of fractional slot single layer stator winding

As an important reduction of the eddy current losses can be obtained by considering segmentation of the magnets [11], several segmented magnets configurations have been evaluated and the corresponding results with the effects of frequency variation are shown in Figs. 8 and 9. These figures illustrate that even under low flux density values and frequencies corresponding to space harmonics at fundamental frequency of 50 Hz the eddy current losses in the permanent magnets are quite important.

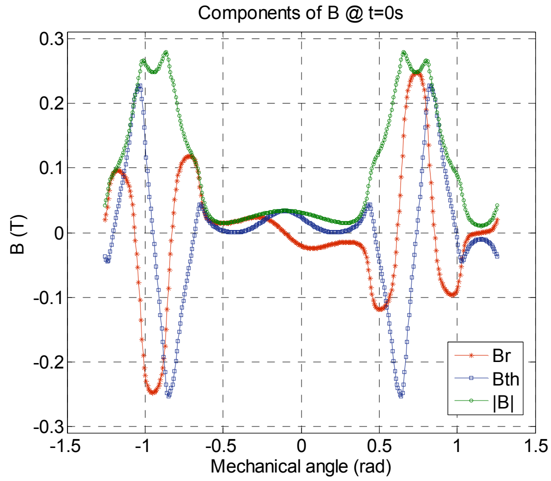

Fig. 7. Flux density components distribution in the air gap surface in case of fractional slot double layer stator winding.

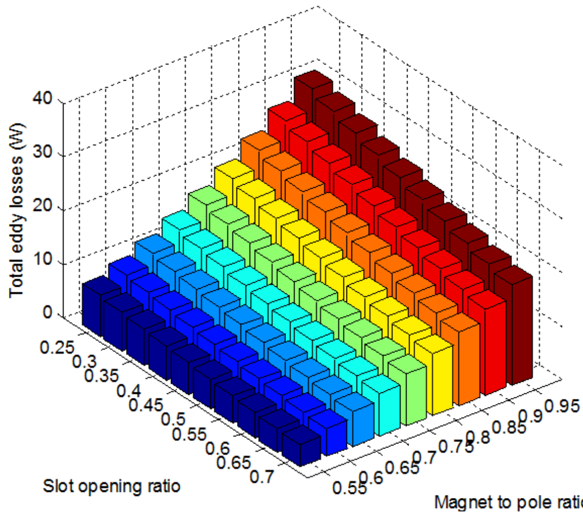

Fig. 8. Eddy current losses variation in the permanent magnets with frequency and magnet segmentation in case of fractional slot single layer stator winding.

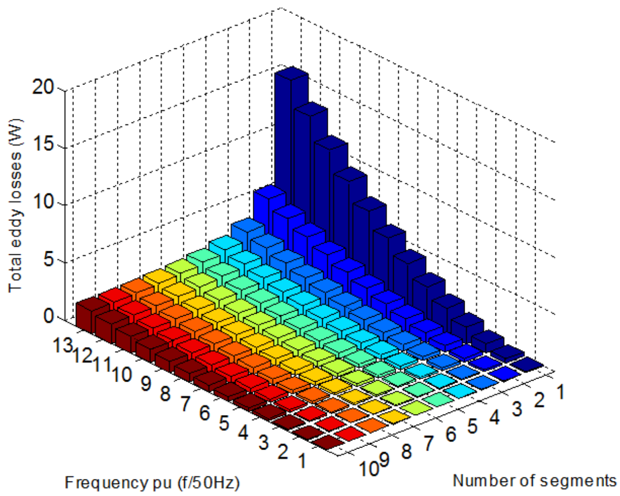

Fig. 9. Eddy current losses variation in the permanent magnets with frequency and magnet segmentation in case of fractional slot double layer stator winding.

C. Consideration of temperature effects on remanence

Permanent magnets present decrease of their remanence with temperature rise and in particular applications involving high temperatures the selection of the magnetic material may constitute a challenge. Consequently adequate representation of permanent magnet materials involves usually a thermal analysis of the problem in conjunction with the electromagnetic one. In the followings an investigation is undertaken among two representative alloys of Neodymium-Iron-Born (NdFeB) magnets presenting higher remanence with less thermal stability in one hand and Samarium-Cobalt (SmCo) alloy, being more stable with temperature and involving less romance in the other. The main data of the two magnets considered are reported in tables I and II. The characteristics in high temperature ranges of the commercially available NdFeB alloy Neomax magnet with those of the SmCo alloy are compared both in terms of magnetic field simulation and experimental validation in magnetic circuits.

Fig. 10. Magnetic circuit of soft magnetic material placed in the chamber with controlled temperature for the experimental validation

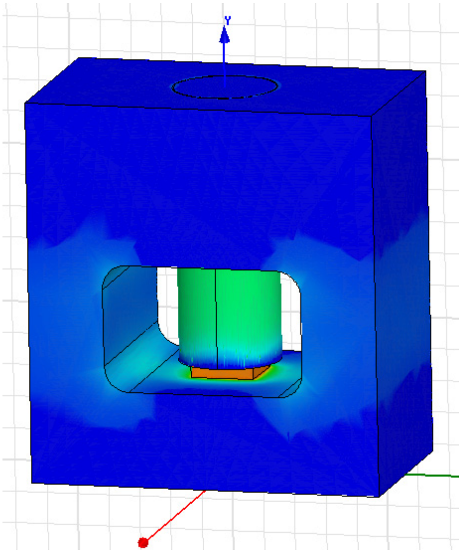

Fig. 11. Geometry of the magnetic circuit and f distribution of the amplitude of the flux density

TABLE I. NEODYMIUM ALLOY PERMANENT MAGNET CHARACTERISTICS.

TYPE	NMX-33UH
Br (mT)	1150
Hcb (kA/m)	852
Hcj (kA/m)	1990
(BH)max (kJ/cm^3)	270
Block dimensions (mm)	10x10x2
Magnetized along	2 mm

The problem has been analyzed by using a variable air-gap magnetic circuit of soft magnetic material with a magnet placed in one side of the gap shown in Figs. 10 and 11. Then the force applied to the moving part of the circuit has been measured for under various temperatures and air-gap widths, enabling determination of the magnetic field with temperature. The simulation has been performed by using 3D FEM analysis and the obtained results have been compared to measurements. Figure 12 shows the adopted mesh while Figs. 11 and 13 illustrate the field distribution in terms of amplitude values and vectors, respectively, for SmCo magnet material and for the operating temperature of 25 ^{o}C (room temperature).

Simulations and experiments were carried out for both PM materials considered and for operating temperatures ranging from 25 ^{o}C to 250 ^{o}C.

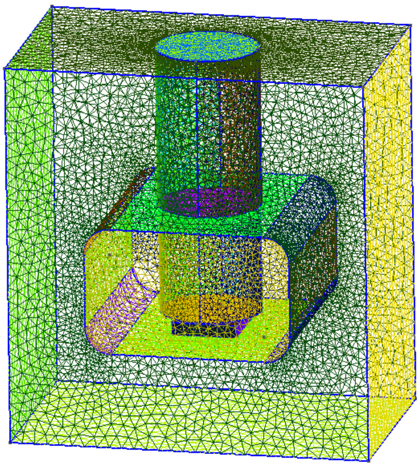

Fig. 12. Mesh implemented in the 3D analysis by using FEM

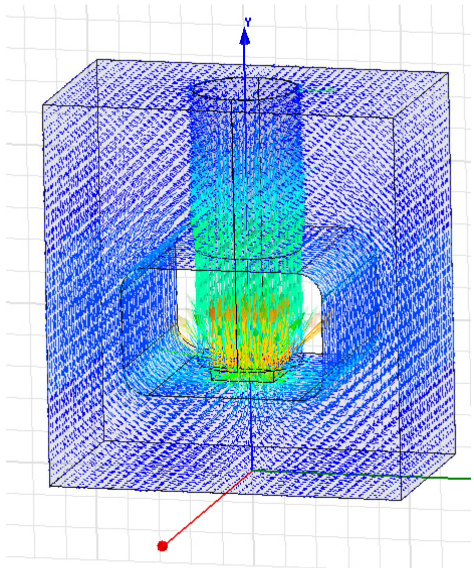

Fig. 13. Vector representation of the flux density distribution in SmCo magnet case at room temperature

TABLE II. SAMARIUM ALLOY PERMANENT MAGNET CHARACTERISTICS.

TYPE	NMX-33UH
Br (mT)	1100
Hcb (kA/m)	820
Hcj (kA/m)	2070
(BH)max (kJ/cm^3)	220
Block dimensions (mm)	10x10x2
Magnetized along	2 mm

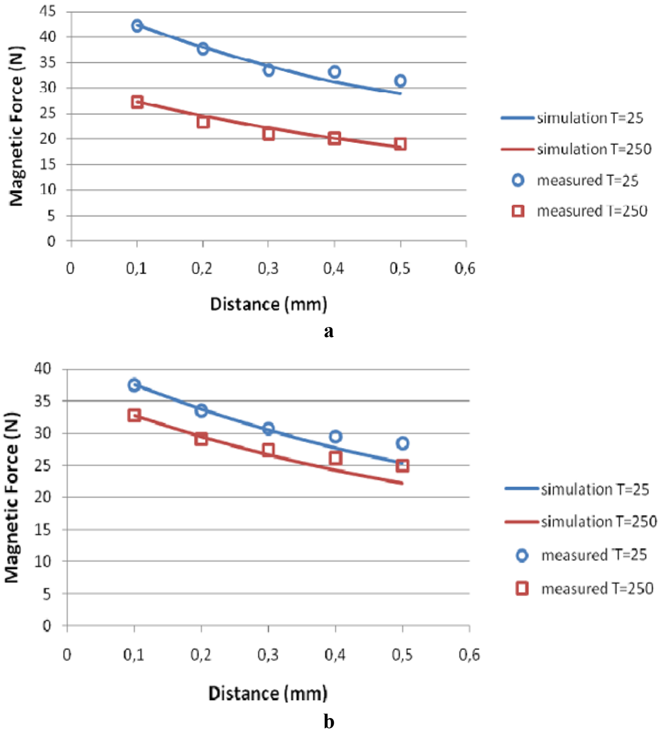

Fig. 14. Comparison of experimental and simulation results for two different operating temperatures (25 °C and 250 °C) and two magnetic materials. a: NdFeB and b: SmCo alloy magnets.

The obtained force results for the extreme temperatures of this investigation are compared in Fig. 14. The thermal behavior and stability of the two materials were investigated and it has been assessed that below 180 °C the tested NdFeB magnets exhibit better characteristics while above 180 °C SmCo magnets are favored. It may be noted that 250 °C is the maximum operating temperature for NdFeB magnets while SmCo magnet temperature withstand is 350 °C.

III. Optimization Procedure

The optimization of electrical machines geometry constitutes a complex procedure involving research of a compromise amongst objective functions of usually adverse criteria representing in general construction cost, operating cost and maintenance cost, respectively. A formal representation of these three main objective functions can be expressed as follows:

$$F=\begin{bmatrix}F_1 & F_2 & F_3\end{bmatrix}=\left[\frac{T_{mean,0}}{T_{mean}} \quad \frac{P_{Cu}+P_{Fe}+P_{Mag}}{\left(P_{Cu}+P_{Fe}+P_{Mag}\right)_0} \quad \left(0.5\cdot\frac{THD_{EMF}}{\left(THD_{EMF}\right)_0}+0.5\cdot\frac{T_{ripple}}{T_{ripple,0}}\right)\right] \tag{10}$$

where the three objective functions F_1, F_2, F_3 correspond to maximization of the mean torque capability T_{mean}, minimization of total copper, iron and permanent magnet losses P_{Cu}, P_{Fe}, P_{Mag}, and minimization of back-EMF harmonic content and torque ripple THD_{EMF}, T_{ripple}, respectively. It may be noted that the index the index 0 refers to the electromagnetic characteristics of an initial design.

The optimizing variables x_j may involve geometrical characteristics as well as operational characteristics such as current loading and temperature developed. In general it is preferred to reduce operational characteristics through inequality constraints. Moreover as the geometrical characteristics are usually numerous, it constitutes an important procedure to limit them as much as possible without affecting the optimization, in order to obtain a feasible optimization scheme. As an example typical geometrical parameters that can be used as design variables in the case of a surface mounted permanent magnet machine are shown in Fig. 15.

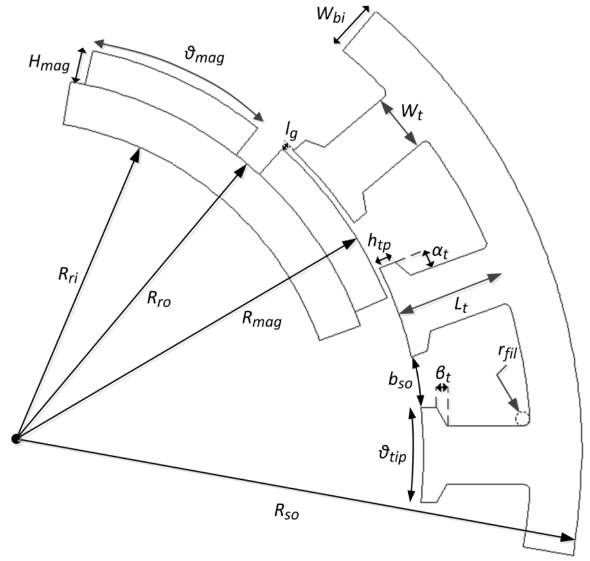

Fig. 15. Main geometrical parameters of a surface permanent magnet machine implemented as design variables.

In many cases the optimization procedure involves minimization of a composite objective function $u(x)$ constituted by adding the m partial cost functions $f_i(x)$ with appropriate weights w_i as follows:

$$u(x)=\sum_{i=1}^{m} w_i f_i(x) \tag{11}$$

while in general a normalization of the weights is considered:

$$\sum_{i=1}^{m} w_i = 1 \tag{12}$$

The determination of appropriate values for the weights is not always easy and such a procedure may lead to suboptimal geometries. Furthermore, the analysis problem has to be solved many times in order to reach convergence that is why such a procedure may be very time consuming if FEM modeling is applied. In order to accelerate the results, at a preliminary stage the optimization can be based on equivalent magnet circuit method, described hereafter.

A. Equivalent Magnetic Circuit Method

The equivalent magnetic circuit method constitutes a distributed magnetic circuit analysis enabling local field evaluation involving reduced computation time with respect to FEM at the expense of less accuracy [22],[23].

In particular the flux leakage effects on air-gap flux distribution, and consequently on electromagnetic torque and back-EMF waveforms can be analyzed [24]. In order to quantify the aforementioned effects, a magnetic equivalent circuit method can be implemented. Figure 16a illustrates the magnetic circuit parts for one stator slot and the respective leakage and magnetizing flux lines in the case of surface mounted permanent magnet machine. Figure 16b depicts the motor topology as a linear translation equivalent and the respective magnetic circuit network. The detailed magnetic circuit network topology is shown in Fig. 17 illustrating the positions of the various elements reluctance. The calculation of magnetic resistances is performed by considering linear iron parts while the distribution of the magnetic flux per pole Φ_r is obtained by simple relations.

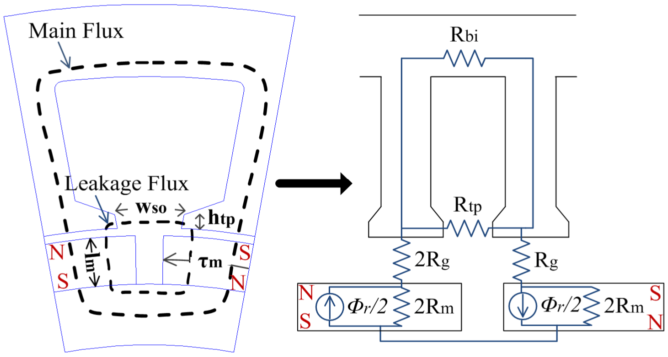

a b

Fig. 16. Equivalent magnetic circuit method implemented in surface mounted permanent magnet machine case.
a: Magnetic circuit for one stator slot b: Magnetic circuit network.

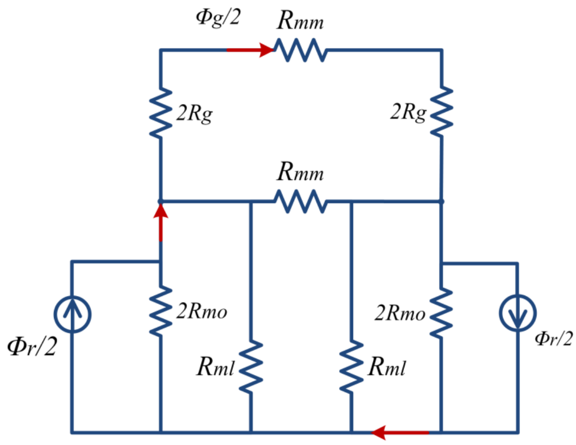

Fig. 17. Equivalent magnetic circuit network of the surface mounted permanent magnet machine case.

B. Pareto Front Analysis

The minimization of composite objective functions with fixed weights necessitates very exact knowledge of the weight contributions and may lead to suboptimal solutions. It is preferable to modify the weight values and investigate the impact on the objective function optima obtained. Such points are pareto front points and their investigation leads to more robust results. Figure 18a illustrates a geometrical representation of pareto front in case of composite convex objective function minimization constituted of two weighted cost functions. The shaded region represents the objective function definition domain. The red lines represent equi-value lines of the cost function and point A belongs to the pareto front for a specific combination of weights while points B and C are the extreme points of the pareto front for values of the weights (1,0) and (0,1), respectively.

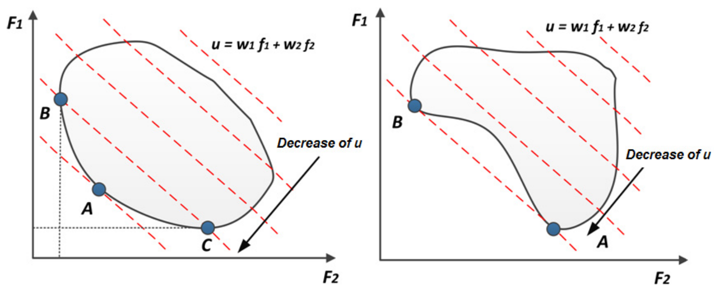

a b

Fig. 18.Geometrical representation of pareto fronts in case of composite objective function minimization constituted of two weighted cost functions.
a: convex objective function b: concave objective function

Figure 18b illustrates in counterparts the case of concave objective function where the pareto front points between A and B cannot be obtained. In order to provide robust solutions when the exact evaluation of the weights of the constitutive cost functions is difficult to perform as well as to identify pareto front points situated in cavities of the objective function evolutionary strategies can be developed based on genetic algorithms, which will be illustrated through the application examples presented in the followings.

IV. Applications

The methodologies developed have been applied in order to improve characteristics of surface mounted permanent magnet motors concerning three electric traction applications:

- Electromagnetic actuator for aerospace applications
- Wheel motor for a small electric vehicle

A. Electromagnetic actuator for aerospace applications

In this application an evolutionary multi-objective optimization algorithm is proposed, facilitating the comparative approach on both the stator and rotor geometry optimization of a Surface Mounted Permanent Magnet Motor (SMPM), involving Fractional Slot Concentrated Winding (FSCW) configuration. The strict nature of the specifications, both operational and spatial, of the application has highlighted the necessity of the thorough investigation of their operational characteristics and behavior as well as their systematized optimization [21].

A Differential Evolution (DE) based optimization algorithm, employing three different optimization criteria, regarding motor performance, motor efficiency and motor clean interface, as mentioned in (10) has been implemented. Three additional optimization constraints are used, rendering the preservation of three cost terms under the specified values. The cost terms are application-specific and account for fill factor, stator tooth-slot shape and tooth-tip flux leakage effect, respectively, thus enabling efficiency, performance and manufacturing cost consideration.

An estimation of the actuator structure has been achieved by considering classical machine design analytical techniques [25]. Such an analytical approach does not enable detailed design optimization, due to the approximate nature of the electromagnetic field representation, but it delivers a sub-optimum set of design variables adequately close to the region of the global optimum. The initial design is focused on the satisfaction of the fundamental spatial limitations and operational specifications. Table III summarizes the basic properties of the actuator.

Table III. Main Actuator Specifications and Dimensions.

Specifications		Dimensions (mm)	
Torque	30 Nm	Motor active length	100
Speed	750 rpm	Stator outer radius	50
Current density	15 A/mm^2	Gap width	0.5
Efficiency	0.85	Rotor inner radius	29
PM material	NdFeB	Rotor outer radius	35.7

The proposed optimization methodology implements a three objective DE based optimization routine, utilizing the concept of Pareto non-domination to produce an optimum solutions front [10],[12]. The latter feeds an automated SMPM motor design script, generating a 2D Finite Element (FE) model corresponding to each optimization run, thus allowing for precise computation of the objective function values. The block diagram of the procedure is illustrated in Fig. 19. The selected design variable vector is:

$$X_G = \begin{bmatrix} W_{t2} & L_{tooth} & h_{tp} & W_{t1} & \theta_{mag} \end{bmatrix}_G \tag{13}$$

where W_{t2} is the stator tooth width, L_{tooth} is the stator tooth length, h_{tp} is the stator tooth tip height, W_{t1} is the stator tooth tip width and θ_{mag} is the magnet angle.

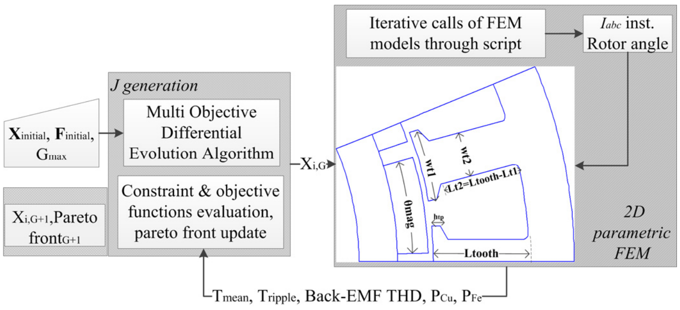

Fig. 18. Overall optimization procedure block diagram.

The flowchart of the implemented DE algorithm and the subroutine of the constraints and objective functions handling in particular, are shown in figures 19a and 19b, respectively. The constraints handling strategy is the "death penalty". For every trial vector generated in each generation, constraint functions are evaluated and the potential population member is immediately rejected if at least a single constraint is violated. If none constraint is violated, the objective functions for the vector are evaluated and selection is performed.

The trial vector is compared in terms of non-domination to the respective current population member and if it enters the current generation population, it competes with all the current Pareto front members, and the front is updated. It should be noted that a new generation member can dominate multiple members of the Pareto, which are eliminated from the front.

In the process of donor formulation, mutation and recombination the standard DE processes are employed [9]. The mutation factor was set equal to F=0.85 and the crossover probability was set equal to FCR=0.8. Forced mutation was used for at least one design variable of every trial vector in order to avoid vector duplication. An additional promotion probability FPND=0.5, that randomly promotes the trial or the current population member to the next generation, if neither dominates, is used.

Three particular cost terms C_1, C_2, C_3 have been introduced in the form of constraints in the optimization routine [24]. The first two account for technical-manufacturing complexity of the actuator design. In particular, the first technical cost term accounts for fill factor and the second for stator tooth-slot shape.

Figure 20 illustrates the variation of the first and second technical cost terms. It has been proved that the integration of manufacturing cost evaluation in the geometrical optimization procedure can significantly improve the performance of actuators, leaving technical costs practically unaffected.

The third technical cost term relates the tooth tip shape and the magnet angle with the resulting leakage flux, in a rather efficient manner. An equivalent magnetic circuit approach was adopted to determine a convenient straightforward interpretation. For the purposes of the analysis, a quick estimation of the flux leakage effect was essential and the magnetic equivalent circuit method yielded adequately precise results without compromising computational efficiency.

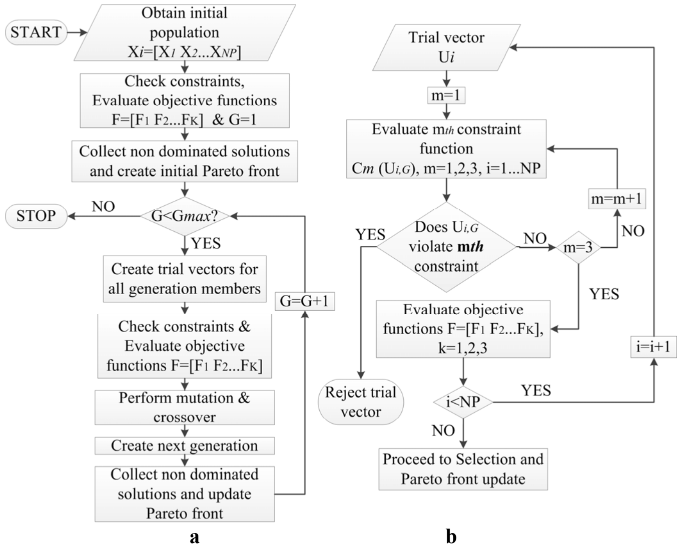

Fig. 19. Flowchart of the implemented algorithm.
a: Overall procedure. b: Constraint and objective function handling.

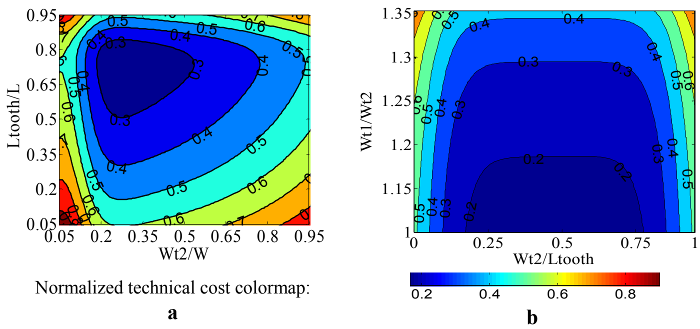

Fig. 20. Technical cost terms variation.
a: C1 term, copper fill factor effect. b: C2 term, stator tooth-slot shape effect.

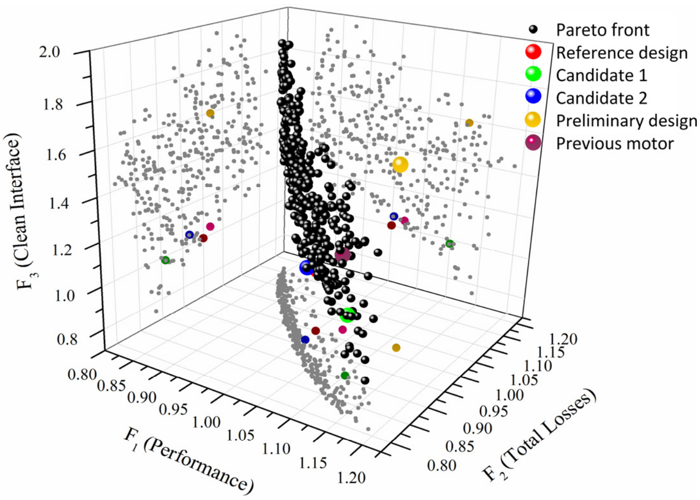

Fig. 21. Final 3D Pareto front and 2D projections of the Pareto front after 48 generations.

The resulting Pareto front in the 3D objective function space is presented in Fig. 21. This Figure also depicts the three projections of the Pareto front on the respective objective function surfaces. From the abovementioned analysis, two new optimal designs occurred. The position of the initial design and the two candidate designs in the objective function 3D space is also indicated. At the end of the optimization procedure, the number of the Pareto front members-optimal solutions reached a value of 343. The conflicting nature of the objective functions is evident from the final shape of the front. The design parameters values for the existing actuator, as well as those for two new optimal designs, each emphasizing on a different criterion, are tabulated in Table IV.

TABLE IV. OPTIMAL DESIGN PARAMETER VALUES.

Variable	*Init. Design*	*Cand. Design 1*	*Cand. Design 2*
Torque	30 Nm	Motor act. length	100 mm
Speed	750 rpm	Stator outer radius	50 mm
Current dens.	15 A/mm^2	Gap width	0.5 mm
Efficiency	0.85	Rotor inner radius	29 mm
PM material	NdFeB	Rotor outer radius	35.8 mm

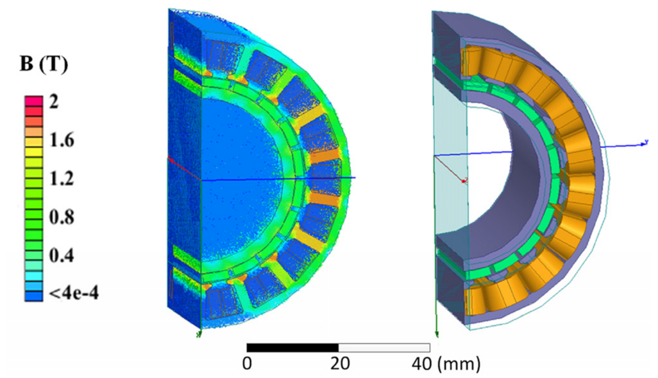

Fig. 22. 3D magnetic field distribution and final motor geometry.

From the two aforementioned optimum designs the second was selected, based on the application demands for increased efficiency and minimum nominal torque capability. An additional 3D electromagnetic and thermal analysis was performed to validate the results obtained by the optimization procedure, for the final selected actuator geometry. The respective 3D motor geometry and magnetic field distribution are illustrated in Fig. 22 while the temperature distribution is shown in Fig. 23. It may be noted that the final optimized design involves 4% increase of the torque and 7% decrease of the losses with respect to the reference one.

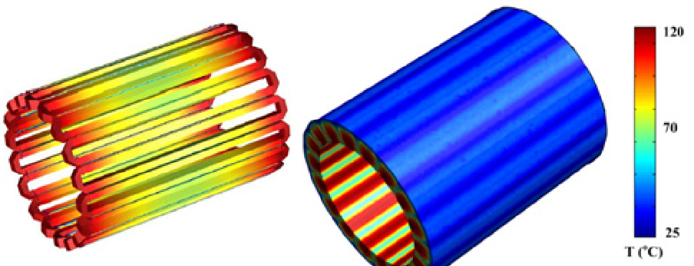

Fig. 23. 3D temperature distribution in the stator windings and core of the final motor geometry

B. Wheel motor for a small electric vehicle

A small vehicle electric motor, appropriate to be placed on a wheel concerning 100 kg weight and 30 km/h speed has been considered. Initially, an estimation of the motor structure is achieved by considering classical machine design, according to specifications and space limitations that are mainly dictated by the in-wheel nature of the motor. On a second step, a hybrid Strength Pareto Evolutionary Algorithm (SPEA) technique, combining features of SPEA and DE, is utilized to optimize the motor geometry on a systematized basis. The improved fitness assignment scheme and the nearest neighbor density estimation method of SPEA 2 are utilized in the algorithm. The raw fitness of every individual is calculated as:

$$R(i) = \sum_{j \in (P^0 + P),\, j \succ i} S(j) \tag{14}$$

where P^0 is the current archive population, P is the current generation population and the symbol $\succ$ corresponds to the Pareto dominance relation. The raw fitness is determined by the strengths of the dominators of a solution both in the Pareto front and the population. The density value assigned to every population member, to discriminate between individuals with identical fitness values, is estimated using the k-*th* nearest neighbor method as:

$$D(i) = \frac{1}{\sigma_i^k + 2} \tag{15}$$

where σ_i^k is the distance of the i-*th* population member to the k-*th* nearest neighbor. The overall fitness value of an individual is calculated as:

$$F(i) = R(i) + D(i) \tag{16}$$

However, the archive truncation method of SPEA 2 has been replaced by the clustering analysis technique of SPEA 1. The preservation of boundary solutions is less critical in such applications where the preliminary design procedure delivers a set of design variables adequately close to the optimum front, contrary to the need for computationally efficient reduction of the archive size.

Additionally, the concept of differential vectors used in DE is employed during the tournament selection to increase trial vector diversity over the mating pool space. In the process of donor formulation, mutation and crossover, the standard DE processes are employed [3]. The mutation factor is set equal to F=0.85 and the crossover probability equal to F_{CR}=0.8. Forced mutation is used for at least one design variable of every trial vector in order to avoid vector duplication. An additional promotion probability F_{PND}=0.5, that randomly promotes the trial or the current population member to the next generation, if neither dominates, is used. The DE strategy employed is the DE/local-to-best/1/bin, where the best so far vector is a randomly selected member of the Pareto front. For every trial vector two difference vectors are utilized as follows:

$$v_{i,G} = x_{i,G} + F\left(x_{best,G} - x_{i,G}\right) + F\left(x_{r2,G} - x_{r3,G}\right) \tag{17}$$

The constraints handling strategy is the “death penalty”. For every trial vector generated in each generation, constraint functions are evaluated and the potential population member is immediately rejected if at least a single constraint is violated. The main problem constraints are the satisfaction of the motor’s minimum torque capacity for nominal and overload conditions and its thermal robustness. For the two aforementioned operating states, the electromagnetic torque versus power angle characteristics are constructed through a series of FE analyses and the torque capacity of the respective geometry for overload and nominal load is calculated. Additionally, a thermal FE model considering the overload condition is used to evaluate the maximum temperature values in the motor magnets and windings [26].

The boundary constraints, regarding the motor’s geometric parameter values, are handled using the bounce-back method. If a trial vector exceeds any of the prescribed bounds, it is replaced by a valid one that satisfies all boundary constraints. The block diagram of the overall optimization procedure is illustrated in Fig. 24.

The selected design vector comprises seven key design parameters and the optimization profile accounts for performance, efficiency and power quality. The selected design variable vector is:

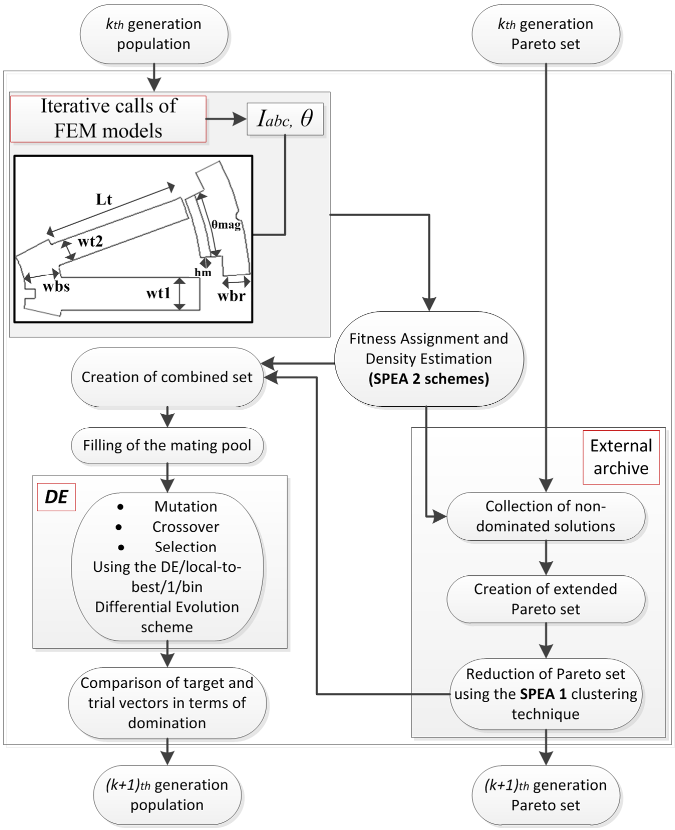

Fig. 24. Optimization procedure main flowchart..

$$X_G = \begin{bmatrix} k_{un} & \theta_{mag} & L_t & W_{t1} & h_{mag} & w_{bs} & w_{bi} \end{bmatrix}_G \qquad (18)$$

where k_{un} is the inequality ratio, θ_{mag} is the magnet angle, L_t is the stator tooth length, W_{t1} is the width of stator thicker tooth, h_{mag} is the magnet height, w_{bs} is the stator back iron thickness and w_{br} is the rotor back iron thickness.

The three objective functions F_1, F_2, F_3 correspond to maximization of torque capability, minimization of total iron, PM eddy and copper losses and minimization of back-EMF harmonic content and torque ripple, respectively (10).

Figure 25a shows the parameterized motor geometry and the main design variables. Figures 25b and 25c depict the concepts of differential vectors and bounce-back boundary constraints handling, utilized in the DE algorithm.

To enable the precise calculation of the temperature distribution in the motor magnets, an analytical model is used to estimate the respective eddy-current losses on the PMs, considering the winding configuration, the basic motor dimensions and the calculated input current of the motors. The relatively small size of the rotor, causing a limited dissipation surface, along with its high power density can incur a significant temperature rise during overload operation, compromising the performance of the motor due to magnets thermal demagnetization [12],[13].

The optimization procedure yielded a set of Pareto optimal solutions set. The final geometry is selected as a tradeoff between weight minimization and efficiency maximization. The resulting Pareto front in the 3D objective function space is presented in Fig. 26. Figure 26 also depicts the three projections of the Pareto front on the respective objective function surfaces. The overall motor weight is considered in the optimization procedure as a selection criterion between the Pareto front members. The weight variation of the resulting optimum motors is also depicted in Fig. 26, using a color map.

The design parameters values for the final selected motor are tabulated in Table V. For the final geometry a 3D thermal model was utilized to validate the results of the 2D model.

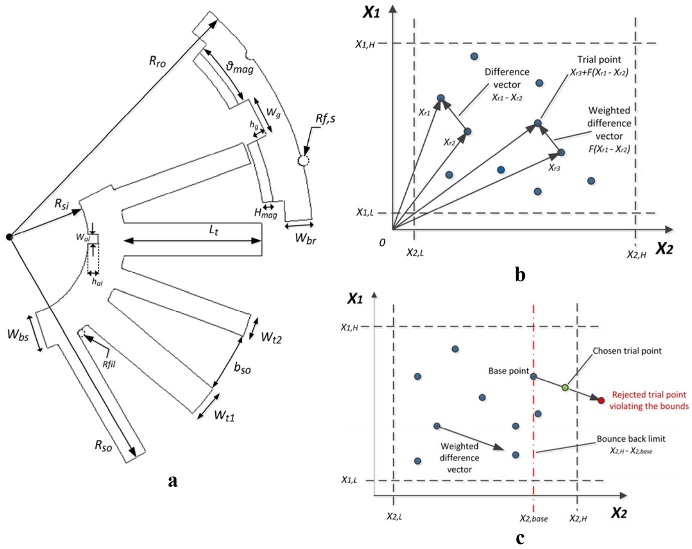

Fig. 25. a: Motor geometry parameterization
b: Visualization the differential vectors.
c: Demonstration of the bounce back constraint handling techniques.

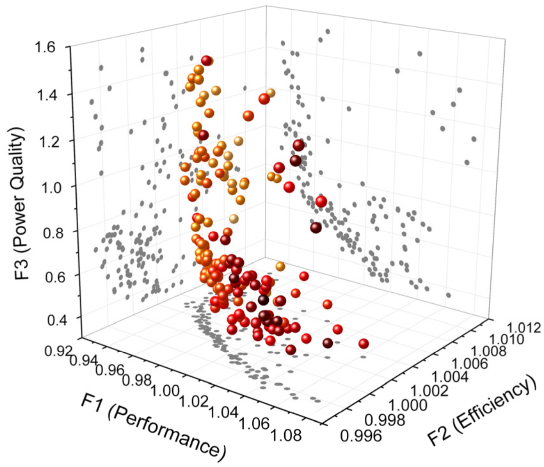

Fig. 26. Optimization results: final Pareto front

TABLE V. OPTIMAL DESIGN PARAMETER VALUES.

Design Variable	Value
Magnet angle (%)	60
Tooth width (mm)	7.00
Back iron stator thickness (mm)	8.00
Back iron rotor thickness (mm)	6.00
Inequality ratio (%)	0.7
Copper Fill factor	0.5
Total mass (kg)	2.95

The constructed housing of the motor is also modeled. The temperature distribution in the motor parts, in extracted view, is illustrated in Fig. 27.

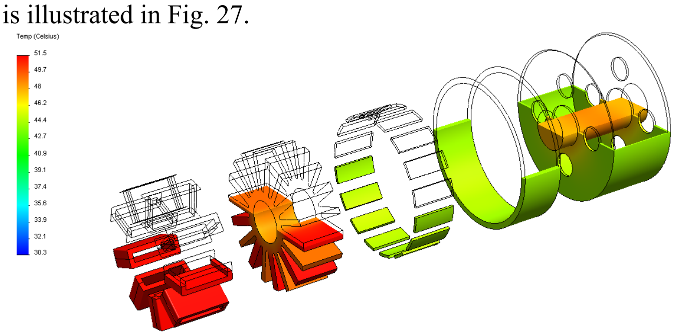

Fig. 27. Results of the 3D thermal model illustrating temperature distribution for overload operation

Actual trends in motor design involve advanced materials, extreme operating conditions concerning current densities, temperatures as well as high speeds that is why the authors believe that the techniques presented concerning analytical eddy current loss evaluation and pareto evolutionary optimization strategies may offer great services.

V. References

[1] Jiabin Wang, Patel, V.I., and Weiya Wang, "Fractional-Slot Permanent Magnet Brushless Machines with Low Space Harmonic Contents," *IEEE Trans. Magn.,* vol. 50, no 1, Jan. 2014, pp. 1-9.

[2] Hafner, M., Finken, T., Felden, M., Hameyer, K., "Automated Virtual Prototyping of Permanent Magnet Synchronous Machines for HEVs," *IEEE Trans. Magn.*, vol. 47, no 5, May 2011, pp. 1018-1021.

[3] Beniakar, M.E., Sarigiannidis, A.G., Kakosimos, P.E., and Kladas, A.G., "Multi-objective Evolutionary Optimization of a Surface Mounted PM Actuator with Fractional Slot Winding for Aerospace Applications," *IEEE Trans. Magn.,* vol. 50, no 2, Feb. 2014, pp. 665-668.

[4] Caravaggi Tenaglia, G., and Lebensztajn, L., "A Multi-objective Approach of Differential Evolution Optimization Applied to Electromagnetic Problems," *IEEE Trans. Magn.*, vol. 50, no 2, Feb. 2014, pp. 625-628.

[5] Coelho, L.D.S., Afonso, L.D., and Alotto, P., "A Modified Imperialist Competitive Algorithm for Optimization in Electromagnetics," *IEEE Trans. Magn.*, vol. 48, no 2, Feb. 2012, pp. 579-582.

[6] Bora, T.C., Coelho, L.D.S., and Lebensztajn, L., "Bat-Inspired Optimization Approach for the Brushless DC Wheel Motor Problem," *IEEE Trans. Magn.*, vol. 48, no 2, Feb. 2012, pp. 947-950.

[7] Gang Lei, Jianguo Zhu, Youguang Guo, Keran Shao and Wei Xu, "Multiobjective Sequential Design Optimization of PM-SMC Motors for Six Sigma Quality Manufacturing," *IEEE Trans. Magn.*, vol. 50, no 2, Feb. 2014, pp.717-720.

[8] Al-Aawar, N., Hijazi, T.M., Arkadan, A.A., "Particle Swarm Optimization of Coupled Electromechanical Systems," *IEEE Trans. Magn.*, vol. 47, no 5, May 2011, pp. 1314-1317.

[9] Di Barba, P., "Evolutionary Multiobjective Optimization Methods for the Shape Design of Industrial Electromagnetic Devices," *IEEE Trans. Magn*., vol. 45, no 3, March 2009, pp. 1436-1441.

[10] Aoyama, Y., Miyata, K. and Ohashi, K., "Simulations and experiments on eddy current in Nd-Fe-B magnet," *IEEE Trans. Magn*., vol. 41, no 10, Oct. 2005, pp. 3790-3792.

[11] Yamazaki, K., Shina, M., Kanou, Y., Miwa, M., and Hagiwara, J., "Effect of eddy current loss reduction by segmentation of magnets in synchronous motors: Difference between interior and surface types," *IEEE Trans. Magn.*, vol. 45, no 10, Oct. 2009, pp. 4756–4756.

[12] Wan-Ying Huang, Bettayeb, A., Kaczmarek, R. and Vannier, J-C., "Optimization of Magnet Segmentation for Reduction of Eddy-Current Losses in Permanent Magnet Synchronous Machine," *IEEE Transactions on Energy Conversion*, vol. 25, no 2, June 2010, pp. 381-387.

[13] Takahashi, N., Shinagawa, H., Miyagi, D., Doi, Y., and Miyata, K., "Analysis of Eddy Current Losses of Segmented Nd–Fe–B Sintered Magnets Considering Contact Resistance," *IEEE Trans. Magn.,* vol. 45, no 3, May 2009, pp. 1234–1237.

[14] Yunkai Huang, Jianning Dong, Long Jin, Jianguo Zhu and Youguang Guo, "Eddy-Current Loss Prediction in the Rotor Magnets of a Permanent Magnet Synchronous Generator With Modular Winding Feeding a Rectifier Load," *IEEE Trans. Magn*., vol. 47, no 10, Oct. 2011, pp. 4203-4206.

[15] Ishak, D., Zhu, Z.Q. and Howe, D., "Eddy-current loss in the rotor magnets of permanent-magnet brushless machines having a fractional number of slots per pole," *IEEE Trans. Magn.*, vol. 41, no 9, Sept. 2005, pp. 2462-2469.

[16] Ruoho, S., Kolehmainen, J., Ikaheimo, J. and Arkkio, A., "Interdependence of Demagnetization, Loading, and Temperature Rise in a Permanent-Magnet Synchronous Motor," *IEEE Trans. Magn.*, vol. 46, no 3, March 2010, pp. 949-953.

[17] Jianning Dong, Yunkai Huang, Long Jin, Heyun Lin and Hui Yang, "Thermal Optimization of a High-Speed Permanent Magnet Motor," *IEEE Trans. Magn.*, vol. 50, no 2, Feb. 2014, pp. 749-752.

[18] Yamazaki, K. and Kanou, Y., "Rotor loss analysis of interior permanent magnet motors using combination of 2-D and 3-D finite element method," *IEEE Trans. Magn.*, vol. 45, no 3, March 2009, pp. 1772-1775.

[19] Krawczyk A., and Tegopoulos J.A., *Numerical modelling of eddy currents*, edited by Oxford University Press, 1993.

[20] Tegopoulos, J.A., and Kriezis E.E., *Eddy currents in linear conducting media*, edited by Elsevier, 1985.

[21] Yunkai Huang, Jianning Dong, Long Jin, Jianguo Zhu and Youguang Guo, "Eddy-Current Loss Prediction in the Rotor Magnets of a Permanent Magnet Synchronous Generator With Modular Winding Feeding a Rectifier Load," *IEEE Trans. Magn.*, vol. 47, no 10, Oct. 2011, pp.4203-4206.

[22] Turowski, J., Turowski, M., Kopec, M., "Method of three-dimensional network solution of leakage field of three-phase transformers," *IEEE Trans. Magn.,* vol. 26, no 5, 1990, pp. 2911- 2919.

[23] Han-Wook Cho, Ju-Seong Yu, Seok-Myeong Jang, Chang-Hyun Kim, Jong-Min Lee, and Hyung-Suk Han, "Equivalent Magnetic Circuit Based Levitation Force Computation of Controlled Permanent Magnet Levitation System," *IEEE Trans. Magn.*, vol. 48, no 11, Nov. 2012, pp. 4038-4041.

[24] Kazan, E., and Onat, A., "Modeling of Air Core Permanent-Magnet Linear Motors With a Simplified Nonlinear Magnetic Analysis," *IEEE Trans. Magn.*, vol. 47, no 6, June 2011, pp. 1753-1763.

[25] Kakosimos, P, Tsampouris, E., Kladas, A, "Design Considerations in Actuators for Aerospace Applications," *IEEE Trans. Magn.*, vol. 49, no 5, May 2913, pp. 2249-2252.

[26] Sarikhani, A., and Mohammed, O.A., "Multiobjective design optimization of coupled PM synchronous motor-drive using physics-based modeling approach," *IEEE Trans. Magn.*, vol. 47, no 5, May 2011, pp. 1266–1269.

Authors Name and Affiliation

Minos E. Beniakar, Antonios G. Kladas, John A. Tegopoulos[1], Laboratory of Electrical Machines and Power Electronics, School of Electrical and Computer Engineering, National Technical University of Athens, 9, Iroon Polytechneiou street, 15780 Athens, Greece. Tel: (+30)-210-7723765, beniakar@central.ntua.gr, kladasel@central.ntua.gr

[1]post mortem